Supporting Information

Catalytic Aqueous Phase Hydrogenation of Ketones Using Activated Carbon Monoliths

Justin Weber[1], Aaron Thompson[2], Jared Wilmoth[2], Bob Gulotty[3], James R. Kastner[1,*]

[1]Biochemical Engineering, College of Engineering
[2]Crop & Soil Sciences, College of Agriculture and Environmental Sciences

The University of Georgia, Athens GA 30602, USA
*Corresponding author phone: 706-583-0155; fax: 706-542-8806

e-mails: jkastner@engr.uga.edu
AaronT@uga.edu

[3]Applied Catalysts/Applied Ceramics Inc., 2 Technology Place
Laurens, SC 29360, Ph: 864-682-2597 x2916
bob.gulotty@appliedcatalysts.com

Supporting Information.

1. Catalyst characterization section.
2. Mössbauer characterization section.
3. Long term ketonization results using red mud
4. Catalytic hydrogenation using ACMC.
5. Identification of compounds in GC/MS Chromatograms for Figure 6.
6. Description of external and internal (or intraparticle) mass transfer calculations.

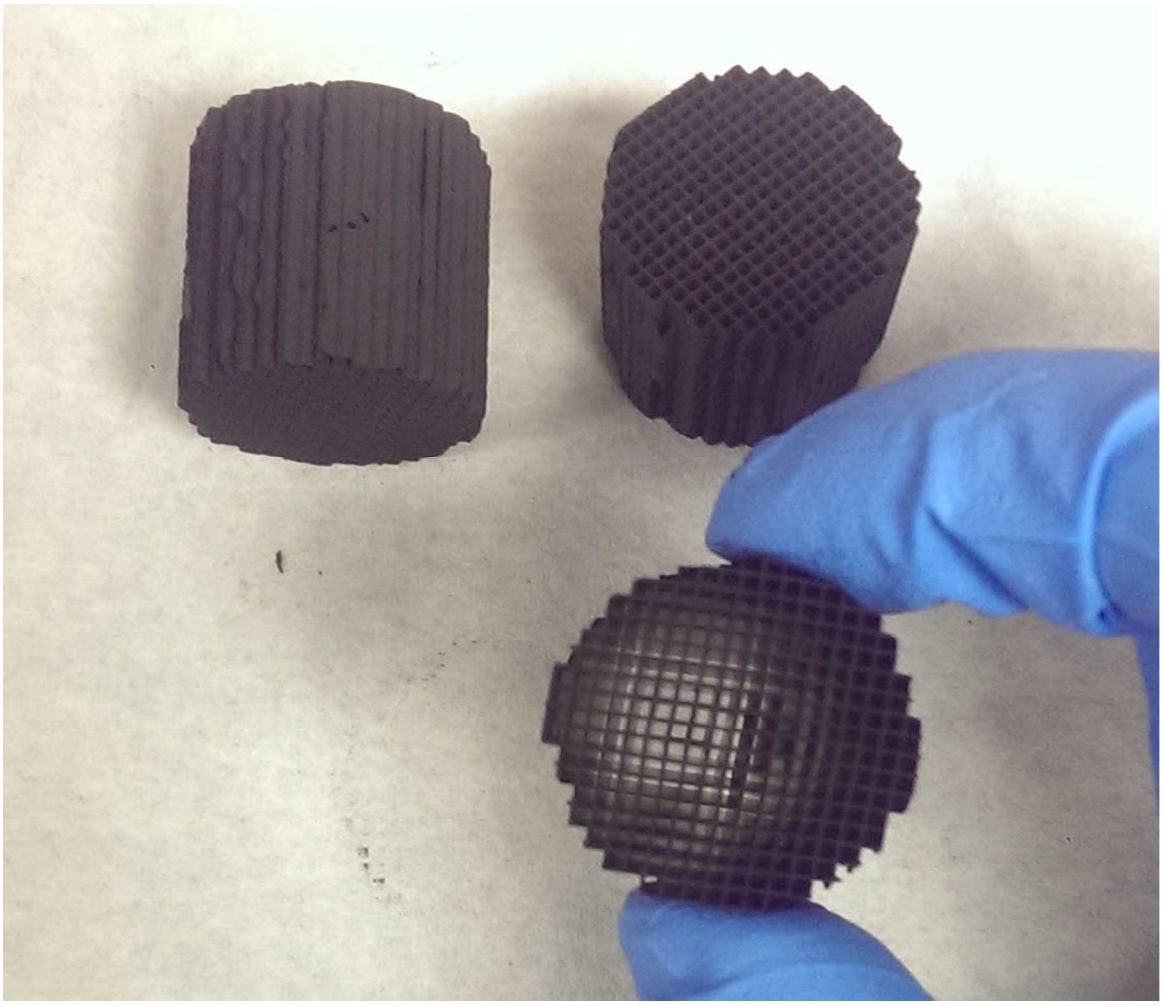

Section 1: *Catalyst Characterization*

Figure S1: Pd carbon monolith cores supplied by Applied Catalysts (Laurens, SC) and used in the catalytic hydrogenation studies (1-in OD, 0.8% Pd, 529 cells/in^2.).

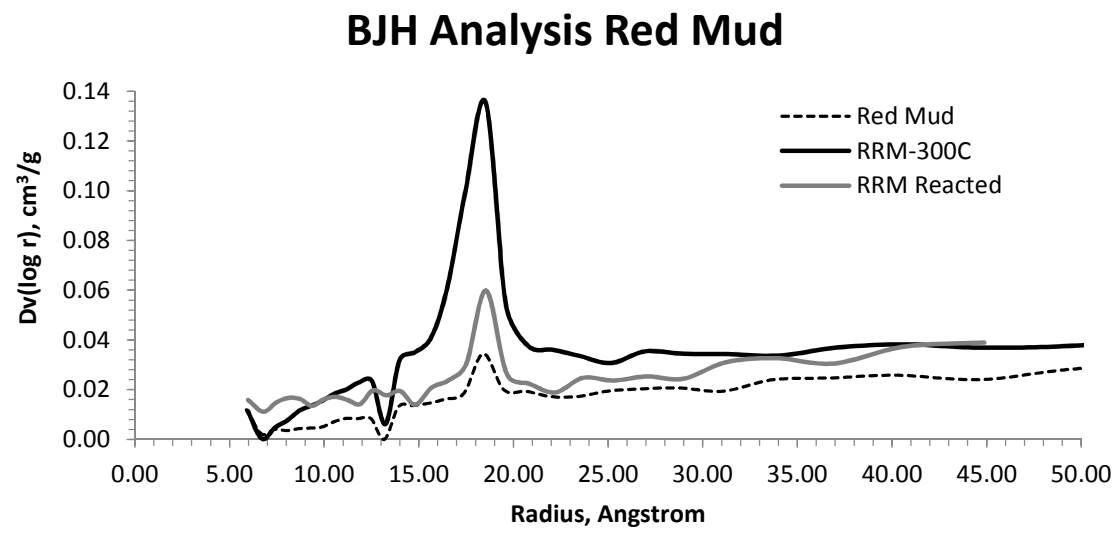

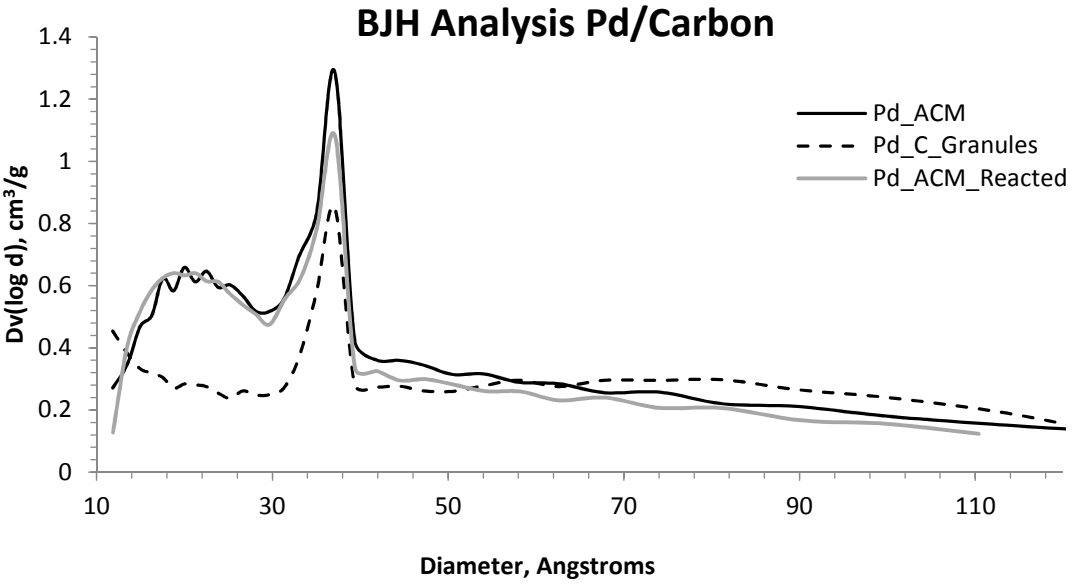

Figure S2: Pore size distribution of RRM (reduced at 300°C for 20 hours), Pd-C granules (5 wt%) without pretreatment, and unused and spent Pd-ACM (0.8 wt%). Spent RRM indicates use in a 6.6 h reaction at 400 °C, P_{atm}, WHSV = 0.21 g/g-cat/hr, and LHSV= 1.41 hr-1. Spent or reacted Pd-ACM was analyzed after approximately 40 continuous hydrogenation reactions over 5 months.

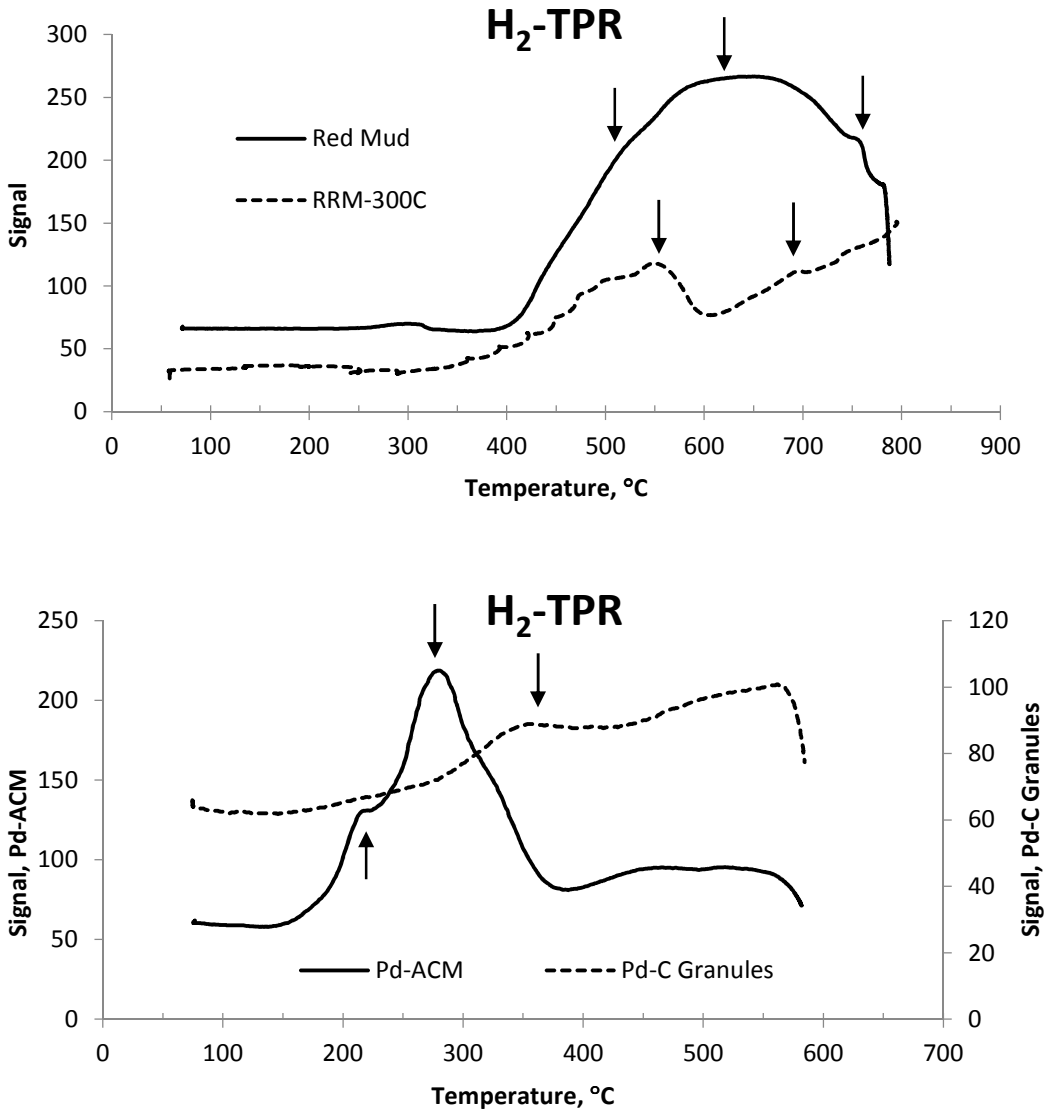

Figure S3: H_2 TPR for untreated red mud, red mud reduced at 300°C, Pd-ACM (0.8 wt. %), and Pd-C (granulated, 5 wt. %). Arrows indicate H_2 reduction reactions.

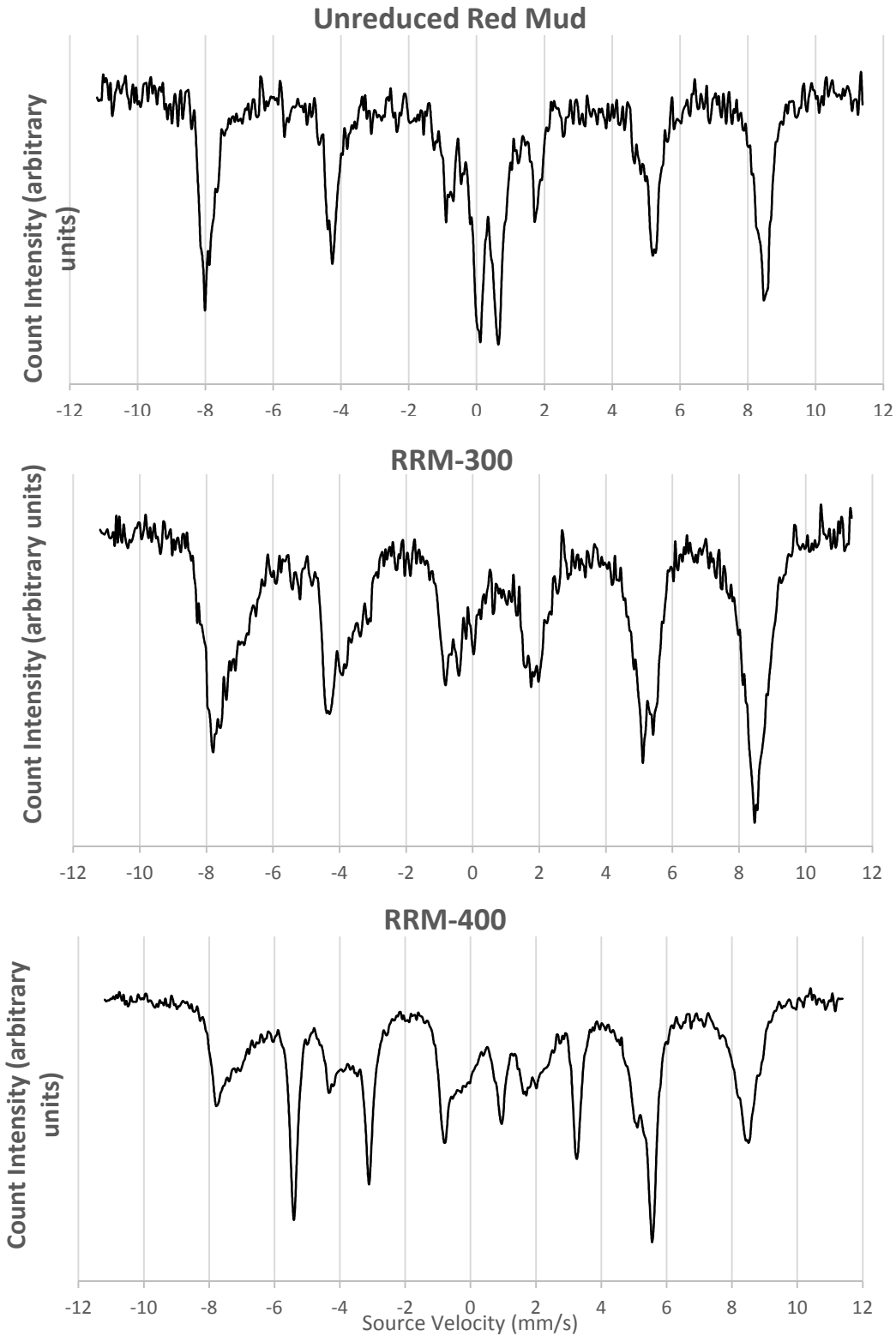

Figure S4: Mössbauer spectrum for unreduced red mud (collected at 295 K) and red mud reduced at 300°C and 400°C, RRM-300 and RRM-400 (collected at 140 K). See SI Section 2 for spectral fitting Table and Figures, as well as additional discussion of the Mössbauer analysis.

Section 2. ^{57}Fe Mössbauer spectroscopy of the Red Mud Samples

SI-2.1 Introduction

We employ ^{57}Fe Mössbauer spectroscopy to evaluate the characteristics of iron in the samples. The unreacted red mud and reduced red mud at 300C and 400C were analyzed at 140K. This temperature was chosen because it is above the Verway transistion for bulk crystalline Magnetite, yet low enough that most Magnetite phases will exhibit the classic two site split. The unreacted red mud sample was also analyzed at 295K and 4K to discern the mineral composition.

SI-2.2 Methods

SI-2.2.1 MB collection and analysis methods

Transmission ^{57}Fe Mössbauer spectroscopy was performed with a variable temperature He-cooled system with a 1024 channel detector. A ^{57}Co source (~50 mCi) embedded in a Rh matrix was used at room temperature. Dried powder samples were mounted between two pieces of 0.127 mm thickness Kapton tape and transferred to the spectrometer. Velocity (i.e., gamma-ray energy) was calibrated using α-Fe foil at 295 K and all center shifts (CSs) and peak positions are reported with respect to this standard. The transducer was operated in constant acceleration mode and folding was performed to achieve a flat background.

SI-2.2.2 MB spectral analysis approach

Mössbauer spectral fitting of all spectra was performed using the Voigt-based fitting (VBF) method of Rancourt and Ping (1991) for quadrupole splitting distributions (QSDs) and combined hyperfine field distributions (HFDs), as implemented in the Recoil^{TM} software, ISA Inc. (http://www.isapps.ca/ recoil). All VBF Mössbauer parameter definitions and a description of the relevant notation are given by Rancourt and Ping(1991). All errors in Mössbauer fitting parameters are two-standard deviation (2σ) errors, as calculated by Recoil^{TM}. In reporting quantitative phase abundances or site populations it is assumed that the Mössbauer recoilless fractions of all detected phases or Fe-bearing components are equal, such that subspectral areas (expressed as fractions of total spectral area) are equal to the amounts of Fe (expressed as fractions of total Fe) in the corresponding phases or components. This assumption is expected to be valid at cryogenic temperatures, and also to be a good approximation at RT with dry samples (Lalonde et al., 1998; Rancourt, 1998).

SI-2.2.3 MB spectral fitting approach

In Mössbauer spectroscopy, each spectral component corresponds to one Fe-bearing solid phase or to a group of unresolved Fe-bearing solid phases. These components take the form of a doublet, sextet, or octet (e.g., for Magnetite) or a collapsed sextet—indicating a Fe-oxide solid-phase near its magnetic ordering temperature (T_N). Fe oxides well above (doublet) or below (sextet) their T_N will not exhibit any vertical (i.e. count axis) distance between the peak troughs and the baseline. When Fe-oxide solid-phases are near their T_N, they exhibit an intermediate shape between a doublet and full sextet, which fills the area between the upper baseline and the

inverse troughs of the peaks. We approximate this by using a separate collapsed sextet component (i.e., a sextet with exceedingly large line widths and Bhf = 0 T).

Assuming equal Mössbauer recoilless fractions (i.e., that the *measurable* gamma rays emitted by each phase are proportional to the phase abundance), the total spectral area of a given component is proportional to the amount of Fe in the corresponding solid phase(s). Furthermore, it can then be assumed that each phase occupies the same spectral area at all temperatures, although not the same spectral shape. For instance, nano-scale Fe^{III}-(oxyhydr)oxide minerals form a doublet at 295K and magnetically order to form a sextet only when cooled sufficiently to prevent thermal disordering of the macroscopic magnetic ordering within the material (Rancourt, 2001).

We left all fitting parameters normally used to fine-tune the fit at their most general, conservative values: These include: constraining all Lorentzian half widths at twice the Heisenberg values; disallowing parameter coupling between the center shift (CS), quadrapole splitting (QS or ε, for sextets) and average hyperfine field (Bhf); and constraining the area ratios between the doublet lines to 1:1 and area ratios between sextet lines 2 and 3 to 2:1 and lines 1 and 3 to 3:1. The exception is the lorentzian half width values, which we set at the value optimized for an α-Fe foil standard on our spectrometer (i.e. 0.1425 mm s^{-1}), which is slightly larger than the ideal theoretical value. An explanation of the four key MB spectral parameters used in our analysis (center shift, quadrapole splitting, hyperfine field strength and the line width) is summarized in the electronic annex of Thompson et al (2011).

SI-2.2.4 Mössbauer spectral components

Across the three collection temperatures (295K, 140K and 4K) we resolved eight distinct spectral components, although not all in each sample (Figures S-1, S-2, and Table S-2). Spectral components include: (1) an Fe^{III} quadrupole doublet (labelled Q-Fe^{III}-1) corresponding to Fe^{III} in silicates, surface-complexed to solids, and in all Fe^{III}-(oxy)hydroxides that are superparamagnetic (SP) at the collection temperature; (2) a broadened Fe^{III} sextet (labelled HFD-OxHy) that corresponds to magnetically-ordered Fe^{III} oxyhydroxides; (3) a partially collapsed Fe^{III} 'sextet' (labelled HFD-(b)Oxhy) due to a Fe^{III}-(oxy)hydroxide having its SP blocking temperature near the collection temperature; (4) a broad sextet (labelled Mag-Site A) with sharp line widths representing FeIII in a tetrahedral position within magnetite; (5) a broad sextet (labelled Mag-Site B) with broader line widths than Mag-Site B that represents the mixture of FeIII and FeII in octahedral positions within magnetite; (6) a broad sextet (labelled Hm-wfm) representing weakly ferromagnetite hematite; (7) a broad sextet (labelled Hm-afm) representing anti-ferrimagnetite hematite; (8) a comparatively narrow sextet (labelled Fe-zero) representing Fe metal. (oxidation state of zero); and (9) a braod sextet (labelled n-Gt) representing nanoparticulate goethite.

SI-2.3. Mössbauer phase analysis

The unreacted Red Mud sample contains two primary iron phases. At 295K (Figure S-2), we resolve a broad sextet with a high field strength and negative quadrapole splitting consistent with crystalline hematite (Bhf=50.9 T, QS= -0.1). At 140K, part of this hematite

population appears to pass through the Morin transition and exhibit a positive quadrapole splitting value of 0.17 mm s^{-1} (Figure S-1), which increases to 0.32 mm s^{-1} when the sample is cooled to ~4K (Figure S-2), but the summed spectral area is similar at each of the temperatures consistent with between 48 and 52% of the iron in the red mud present as hematite (Table S-2). The remainder of the iron in the unreacted sample is present as superparamagnetic Fe (oxy)hydroxide phases, most likely nano-particulate goethite based on spectral parameters at 4K (Figure SI-x). These phases are superparamagnetic (sp) yielding a doublet in the Mössbauer spectra unless cooled below their Neel temperatures. At 295K these phases occupy the central doublet (Q-FeIII-1) and the collapsed sextet (HFD-(b)OxHy), with the later representing the more crystalline portion of that population. At 140K, a significant fraction of the Fe-(oxy)hydroxides has magnetitically ordered (passed below the T_N) yielding a sextet (Fe-OxHy) that comprises 30% of the iron in the sample. By ~4K, the remainder of the the Fe oxyhydroxides have magnetically ordered with MBS parameters in line with nano-goethite (Table S-2).

The Red Mud that is reduced at 300 C, exhibits sextets consistent with 74% of total iron as non-stoichiometric magnetite with A sites representing 34% of total Fe and B sites representing 40% of total Fe. The width of these sextets are a little larger than expected for pure magnetite, with the center shift for the B-sites suggesting more Fe(II) ions than Fe(III) ions (ideal would 0.67 mm s-1, this sample has B-site CS=0.76 mm s-1). The remainder of the iron (~26%) is modelled as a collapsed sextet (HFD-(b)OxHy), which could reflect Fe(III) atoms in short-range-ordered (SRO) Fe phases associated with the magnetite, but prevented from forming a sextet at this temperature due to ion substitutions or small particle size. It may also represent some of the original Red Mud iron that did not transform to Magnetite during the reduction process (i.e. the unreacted Red Mud had 19% of iron present in this component).

The Red Mud that is reduced at 400 C exhibits a similar abundance of SRO Fe phases (HFD-(b)OxHy) as the red mud reduced at 300 C. It also contains ~48% non-Magnetite (split 21% to the A sites and 27% to the B sites), but in addition has ~30% of total iron as zero-valent iron (Fe(0)), which exhibits a low-field strength sextet (Bhf~34T with near zero CS and QS values).

Table S-2: Mössbauer parameters and site populations for the Red mud samples

Sample	Phase	Spectral Area	<CS> or δ_0	< ε >	P	Δ or H	σ	<QS> or <H>	*Red-X²*
		%	mm/s	mm/s	%	mm/s or T	mm/s or T	mm/s or T	
Un-altered Red Mud	Q-Fe^{III}-1	19.0(11)	0.345(11)	n/a	100*	0.571(19)	0.119(40)		0.75
295K	Hm-wfm	52.0(19)	0.3664(81)	-0.1058(81)	100*	50.877(66)	0.954(91)		
(BG = 0.8 MC/ch)	HFD-(b)OxHy	29.1(23)	0.35*	0*	100*	0*	32*		
Un-altered Red Mud	Q-Fe^{III}-1	2.51(78)	0.418(50)	n/a	100*	0.602(88)	0.14(17)		0.71
140K (1Q, 4H)	Hm-wfm	32.5(19)	0.462423*	-0.100081*	100*	52.5157*	0.630701*		
	Hm-afm	16.5(13)	0.449006*	0.17522*	100*	53.0848*	1.09916*		
	Fe-OxHy	29.5(25)	0.473(30)	-0.121(29)	100*	45.76(37)	3.87(46)		
(BG = 1.26 MC/ch)	HFD-(b)OxHy	19.0(31)	0.4*	0*	100*	0*	36(10)		
Un-altered Red Mud	Hm-wfm	30.4(23)	0.4827(54)	-0.0789(74)	100*	53.155(46)	0.35(11)		1.4
5K (3H)	n-Gt	48.0(22)	0.4302(73)	-0.1885(96)	100*	50.45(13)	1.55(14)		
(BG =1.32 MC/ch)	Hm-afm	21.5(18)	0.567(11)	0.323(16)	100*	52.50(11)	0.88(14)		
RRM-300C	Mag-Site-A	34.3(23)	0.386(13)	-0.018(11)	100*	50.55(10)	1.31(13)		0.93
140K	Mag-Site-B	39.6(26)	0.758(29)	-0.059(25)	100*	48.24(24)	3.28(26)		
(BG =1.02 MC/ch)	HFD-(b)OxHy	26.2(30)	0.35*	0*	100*	0*	33.4(62)		
RRM-400C	Mag-Site-A	20.91(79)	0.3939(76)	-0.0026(70)	100*	50.101(62)	1.180(82)		2.13
140K	Mag-Site-B	26.7(11)	0.783(19)	-0.077(17)	100*	47.24(17)	3.76(19)		
	Fe-zero	29.68(74)	0.0820(26)	-0.0001(26)	100*	34.027(18)	0.07(16)		
(BG =4.10 MC/ch)	HFD-(b)OxHy	22.7(12)	0.35*	0*	100*	0*	25.0(22)		

Notes

All fits performed using the Voigt-based fitting method of Rancourt and Ping (1991) with the Recoil™ software.

All fitting and calculated parameters are as defined in by Rancourt and Ping (1991).

All delta-1 couplings between CS and z (or DELTA) were taken to be zero.

All line-1 to line-2 area ratios in all (distributed) elemental doublets were taken to be 1.

All line-2/line-3 and line-1/line-3 area ratios in all (distributed and symmetric) elemental sextets were taken to be 2 and 3, respectively.

All epsilon-1 couplings between epsilon and z (in a HFD) are taken to be 0.

All Lorentzian half widths at half maximum (HWHM) are set at 0.1425 mm/s as measured on Fe foil standards on the instrument.

All center shifts <CS> are given with respect to the CS of metallic Fe at 295K.

BG = background level, in mega-counts per channel (MC/ch).

phase = assigned spectral component, as described in the text.

<CS> = the center shift of a Gaussian component in the quadrupole splitting distribution (QSD) of the hyperfine field distribution (HFD) of a given spectral component.

z = the center (or position) of a Gaussian component in the hyperfine field distribution (HFD) of a given 'sextet' spectral component.

σ = the Gaussian standard deviation width of a given Gaussian component of a given QSD or HFD.

p (in %) is the weight factor for a given Gaussian component in a given QSD or HFD.

<H> is the average magnitude of the hyperfine field (expressed as an excited state Zeeman splitting, in mm/s) in a given HFD of a given sextet spectral component.

Δ is the average magnitude of the quadrupole splitting in a given QSD of a given doublet spectral component.

< ε > is the average magnitude of the slave distribution of quadrupole shifts (epsilons) associated to a given HFD of a given sextet spectral component.

Red-X2 is the reduced chi-squared value for the fit: chi-squared divided by the number of degrees of freedom. It has an ideal value of 1 for a correct model.

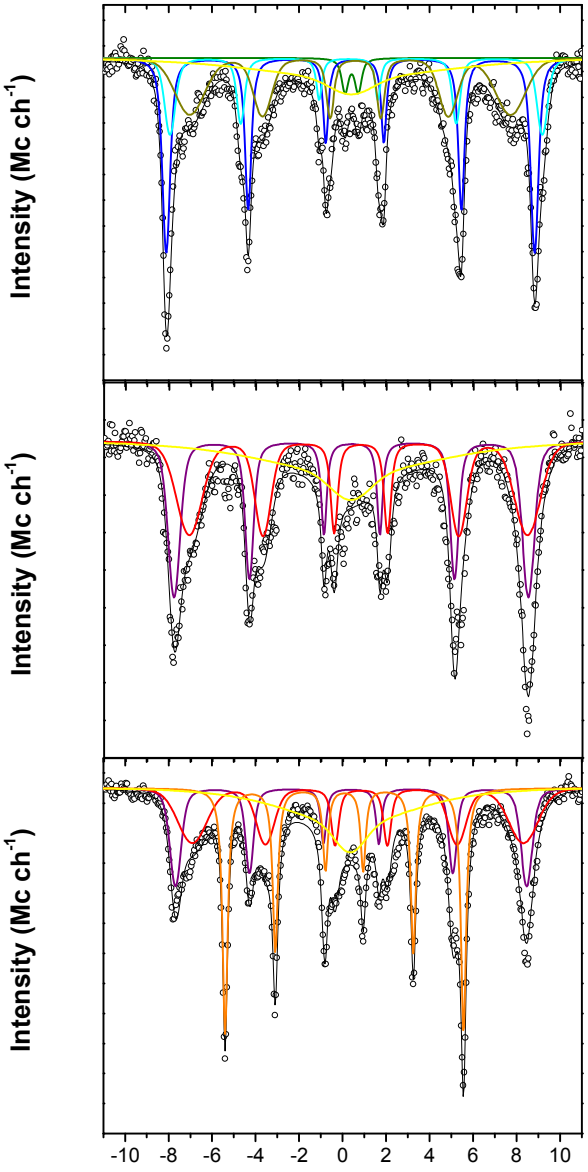

Figure S5. ^{57}Fe Mössbauer spectra at 140K of the **unreacted Red Mud (top spectra), Red mud Reduced at 300C (middle spectra), and Red Mud reduced at 400C (bottom spectra)**. In each spectrum, the black solid line is the total calculated fit, through the discrete data points. The resolved spectral components and assignments are: (1) Q-Fe^{III}-1, the central Fe^{III} quadrupole doublet (blue line in the top spectra); (2) HFD-OxHy, a broadened Fe^{III} sextet (dark yellow line in the top spectra); (3) HFD-(b)Oxhy, a partially collapsed Fe^{III} 'sextet' (yellow line in all spectras; (4) Mag-Site-A, a broad Fe(III) sextet with sharp line widths representing tetrahedral FeIII in magnetite (Magenta line middle and bottom spectras); (5) Mag-Site B, a broad Fe(III) sextet with broader line widths than Mag-Site A (red line middle and bottom spectras) representing FeIII and FeII in octahedral positions within magnetite; (6) Hm-wfm, a broad sextet (purple line top spectra) (7) Hm-afm, a broad sextet (cyan line top spectra); and (8) Fe-zero, a comparatively narrow sextet (orange line bottom spectra).

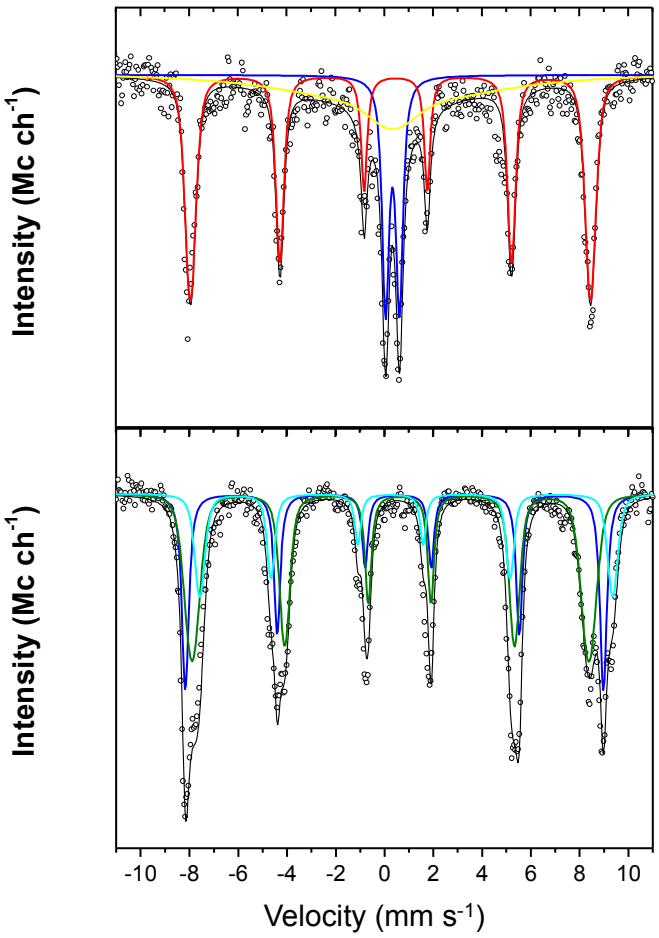

Figure S6. ^{57}Fe Mössbauer spectra at 295K (top) and 4K (bottom) of the **unreacted Red Mud**. The black solid line is the total calculated fit, through the discrete data points. The resolved spectral components are: (1) Q-Fe^{III}-1, the central Fe^{III} quadrupole doublet (blue line, top graph); (2) HFD-(b)Oxhy, a partially collapsed Fe^{III} 'sextet' (yellow line, top graph); (3) Hm-wfm, a broad sextet (orange line, top graph and blue line bottom graph); (4) Hm-afm, a broad sextet (cyan line, bottom graph); (5) n-Gt, a broad sextet (green line, bottom graph).

SI-Section 2 References

Lalonde, A. E., Rancourt, D. G., and Ping, J. Y., 1998. Accuracy of ferric/ferrous determinations in micas: A comparison of Mössbauer spectroscopy and the Pratt and Wilson wet-chemical methods. *Hyperfine Interact.* **117**, 175-204.

Murad, E., 1998. Clays and clay minerals: What can Mössbauer spectroscopy do to help understand them? *Hyperfine Interactions* **117**, 39-70.

Murad, E. and Cashion, J., 2004. *Mössbauer Spectroscopy of Environmental Materials and their Industrial Utilization*. Kluwer Academic Publishers Group, Norwell, Massachusetts.

Murad, E. and Wagner, U., 1994. Mössbauer study of pure illite and its firing products. *Hyperfine Interact.* **91**, 685-688.

Rancourt, D. G., 1998. Mössbauer spectroscopy in clay science. *Hyperfine Interact.* **117**, 3-38.

Rancourt, D. G. and Ping, J. Y., 1991. Voigt-Based Methods For Arbitrary-Shape Static Hyperfine Parameter Distributions In Mössbauer-Spectroscopy. *Nucl. Instrum. Methods Phys. Res., Sect. B* **58**, 85-97.

Rancourt, D. G., Thibault, P.-J., Mavrocordatos, D., and Lamarche, G., 2005. Hydrous ferric oxide precipitation in the presence of nonmetabolizing bacteria: Constraints on the mechanism of a biotic effect. *Geochim. Cosmochim. Acta* **69**, 553-577.

Thompson, A., Rancourt, D. G., Chadwick, O. A., and Chorover, J., 2011. Iron solid-phase differentiation along a redox gradient in basaltic soils. *Geochim. Cosmochim. Acta* **75**, 119-133.

Section 3: *Ketonization Results*

Table S1: Comparison of catalytic results generated from different batches of reduced red mud (RRM-300) 1 year apart.

Date	6/6/2013[a]	08/04/14[b]	6/6/2013[a]	08/04/14[b]
W/F (g-cat/g*h)	1.38 ± 0.33		2.75 ± 0.65	
T, °C	400		400	
Fractional Conversion				
Acetic Acid	0.80 ± 0.12		1.00 ± 0.01	
Formic Acid	0.98 ± 0.05		1.00 ± 0.00	
Acetol	0.80 ± 0.02		1.00 ± 0.00	
Levoglucosan	0.97		1.00	
Yield (mol/mol)				
Acetone	7.29 ± 2.95		7.72 ± 2.73	
2-Butanone	1.10 ± 1.00		2.10 ± 0.25	
Reaction Rate (mmol/g-cat/h)				
Acetic Acid	2.89 ± 0.54		1.79 ± 0.09	
Formic Acid	4.81 ± 0.15		2.46 ± 0.19	
Acetol	2.02 ± 0.10		1.26 ± 0.10	
Levoglucosan	1.28		0.66	

[a,] The runs on 6/6/13 contained 4% acetic, formic, and acetol

[b], The runs on 8/4/14 contained 4% acetic, formic, acetol, and levoglucosan

Error based on range of duplicate experiments and analysis

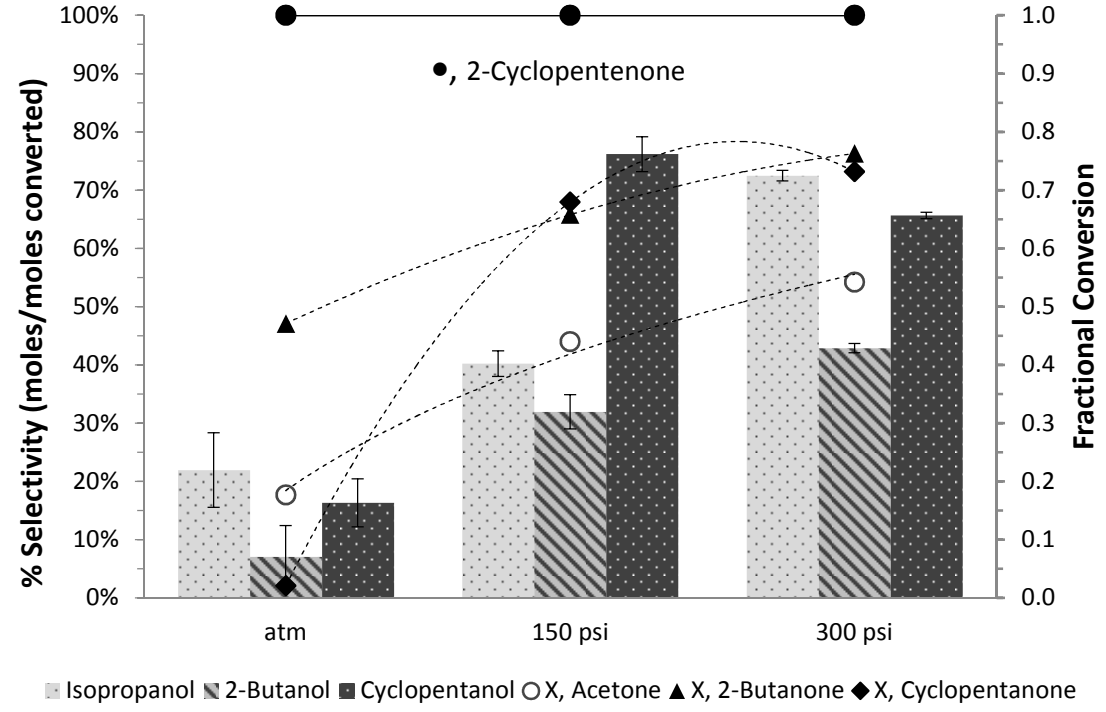

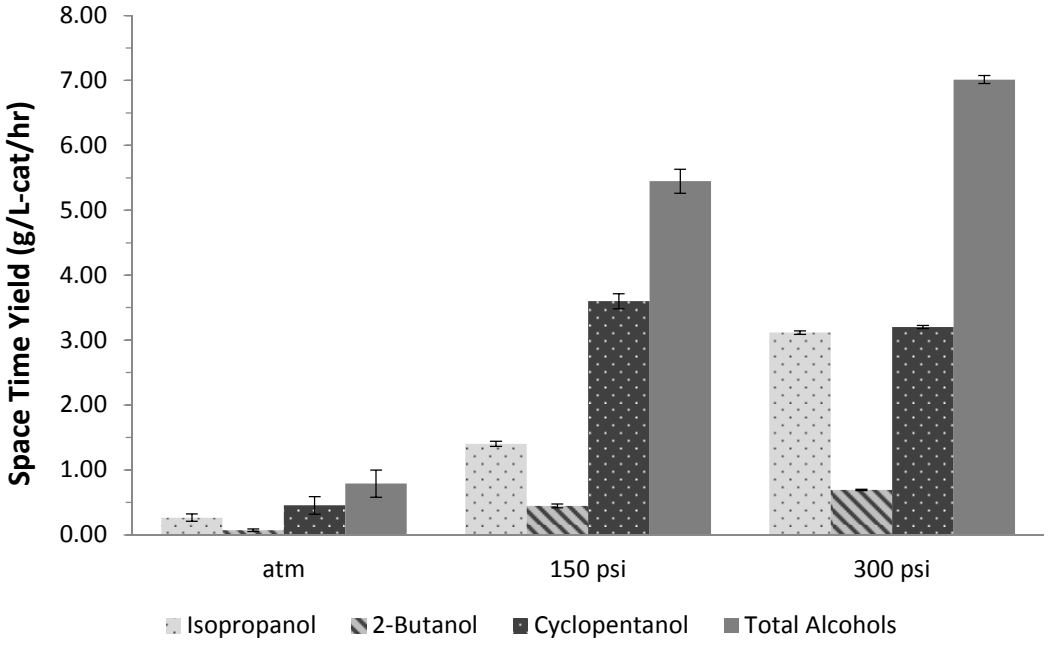

Figure S7: Effect of pressure on catalytic hydrogenation of ketones using Pd-ACM (0.8 wt%, 180 °C, WHSV of 0.0538 hr^{-1}, LHSV of 0.389 hr^{-1}).

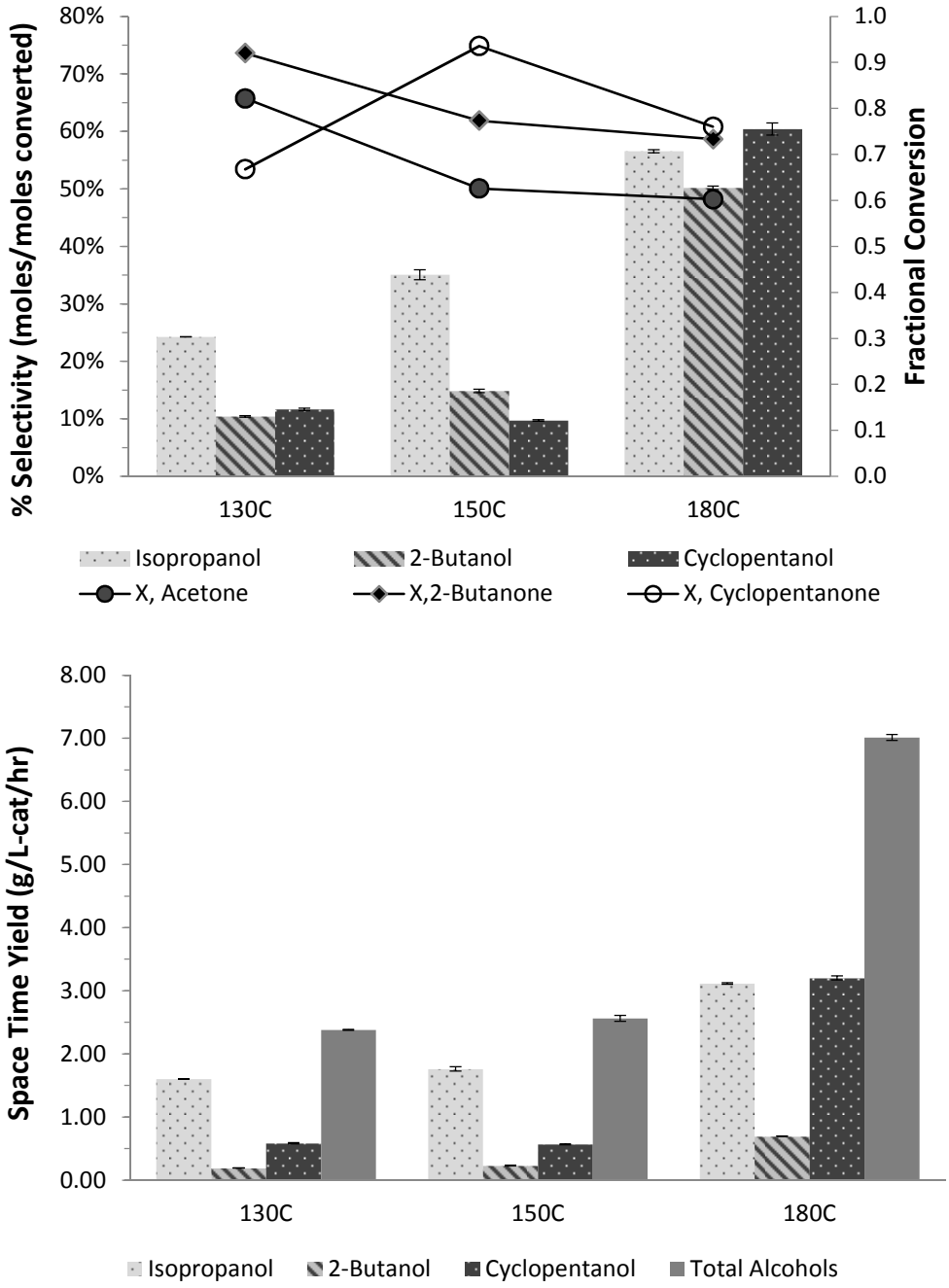

Figure S8: Effect of temperature on catalytic hydrogenation of ketones using Pd-ACM (0.8 wt%, 300 psi, WHSV of 0.0538 hr^{-1}, LHSV of 0.389 hr^{-1}).

Section 5 and Table S2 – GC/MS identification of products formed from catalytic ketonization and hydrogenation using RRM, Pd-C granules, and Pd-ACM from Figure 6 in manuscript. Please note that peak 11 (identified as acetic acid via MS) shifted significantly in each chromatogram (Fig. S9). We thus conclude the ID of this peak is in error or there is a co-eluting compound.

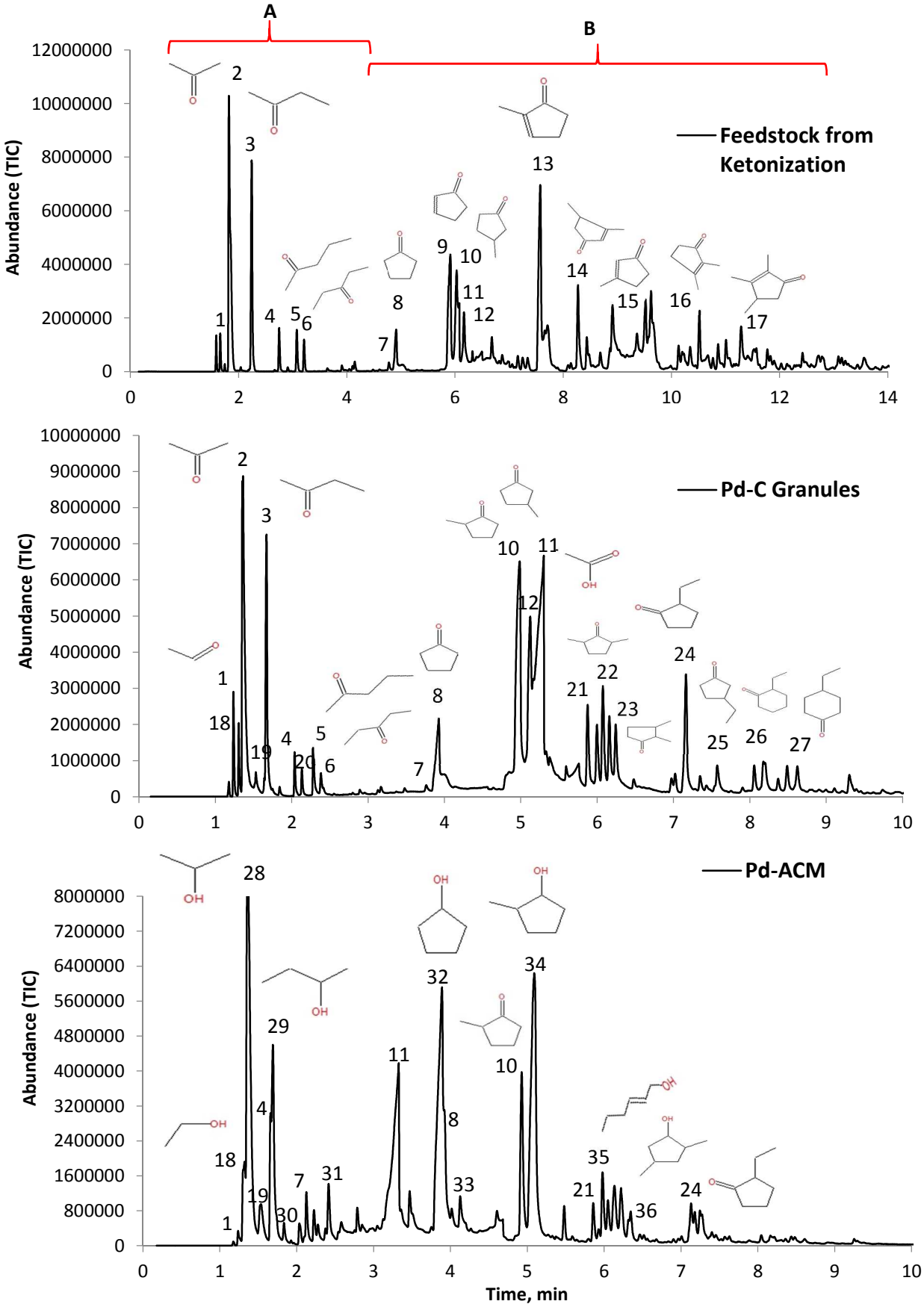

Figure S9: Comparison of GC/MS chromatograms for the feedstock (from ketonization reaction with RRM) and products from granulated Pd-C (5 wt% Pd) and Pd-ACM catalysts (0.8 wt% Pd) in 2nd stage hydrogenation reaction using liquid products from ketonization as feedstocks at 180°C, 300 psi (H_2), and LHSV= 0.78 hr-1. **A** indicates the range of linear ketones and **B** the range of cyclic ketones in the feedstock. Identification of products and GC/MS match factors are presented in Table S1 of supporting material.

Table S2- GC/MS identification of products formed from catalytic ketonization and hydrogenation using RRM, Pd-C granules, and Pd-ACM from Figure S9.

GC/MS ID Catalyst/Reaction/Compound	Number	RMatch[a]	Prob[a] (%)	Comments
RRM/Ketonization				
Acetaldehyde	1	894	75.2	
Acetone	2	959	86.9	
2-Butanone	3	942	87.3	
2-Butanone, 3-methyl-	4	888	56.2	
2-Pentanone	5	932	89	
3-Pentanone	6	963	94	
3-Hexanone	7	922	70.2	
Cyclopentanone	8	881	50.9	4 out of top 5 hits
2-Cyclopenten-1-one	9	928	81.3	
Cyclopentanone, 2-methyl-	10	941	55.2	
Acetic Acid	11	958	93	
3-Methylcyclopentanone	12	897	27.9	3 out of top 5 hits
2-Cyclopenten-1-one, 2-methyl-	13	949	84.5	
2-Cyclopenten-1-one, 3,4-dimethyl-	14	914	51.8	
2-Cyclopenten-1-one, 3-methyl-	15	901	69.7	
2-Cyclopenten-1-one, 2,3-dimethyl-	16	898	62.9	
2-Cyclopenten-1-one, 2,3,4-trimethyl-	17	936	62.3	
Pd-C Granules/Hydrogenation				
Ethanol	18	972	97.6	
1-Propanol	19	861	89.4	
Furan, tetrahydro-2-methyl-	20	944	75.5	
Cyclopentanone, 2,5-dimethyl-	21	911	51.8	
Cyclopentanone, 2,4-dimethyl-	22	890	45.4	
Cyclopentanone, 2,3-dimethyl-	23	848	25.2	
Cyclopentanone, 2-ethyl-	24	946	72.8	
3-Ethylcyclopentanone	25	910	33.5	
Cyclohexanone, 2-ethyl-	26	854	28.8	
Cyclohexanone, 4-ethyl-	27	865	17.3	
Pd-ACM/Hydrogenation				
Isopropanol	28	903	91.8	
2-Butanol	29	932	56.1	7 out of top 10 hits
Furan, tetrahydro-	30	842	39.8	
2-Pentanol	31	774	8.51	
Cyclopentanol	32	862	36	
2-Hexanol	33	882	38.6	
Cyclopentanol, 2-methyl-	34	903	27.6	top 4 hits
2-Hexen-1-ol,	35	818	13.8	5 out of top 8 hits
2,4-Dimethylcyclopentanol	36	839	39.7	

a, see next page

a,

Mass Spectral Analysis. Identification of products in the condensed liquid outlet was based on GC/MS matching with a NIST database and then retention time matching using purchased standards on the GC/MS using the HP-5 column and on an Innowax column using the GC/FID. For intermediates and products identified by GC/MS that could not be purchased, we report match factors with the NIST database for these compounds. Two match factors are reported, a reverse search ignoring peaks in the unknown not in the library spectrum (RMatch) and a probability value (Prob.%). The probability value assumes the unknown is represented by a spectrum in the library and employs the differences between adjacent hits in the hit list to get the relative probability that any hit in the hit lists is correct. In general, according to NIST, 900 or greater is an excellent match; 800–900, a good match; 700–800, a fair match. Less than 600 is a very poor match.

Section 6: *Mass Transfer Effect Calculations*

S6.1 Packed Bed Reactor

Catalytic hydrogenation using the Pd/C particles in the PBR were treated as a trickle bed reactor. In such a system we viewed transport from the bulk liquid to catalyst surface (external resistance) and diffusion and reaction in the porous Pd/C (internal resistance) as the two major resistances to mass transfer that could account for the differences in observed reaction rates and selectivity between the Pd/C and Pd/ACM catalysts. Given the particle size of the Pd/C catalysts ($d_p \leq 0.5$ mm), high surface area (500-600 $m^2\ g^{-1}$) and pore volume (Table 1), we suspected that external and internal mass transfer resistance may have altered ketone hydrogenation relative to the monolith, thus criterion (eqs. 1 and 4) for external and internal diffusion were calculated (Fogler, 1986). According to the Mears criterion if the calculated value is less than 0.15, external mass transfer effects can be neglected (eq. 1).

$$\frac{r_{ketone}\rho_b Rn}{k_c C_{ketone}} < 0.15 \qquad (1)$$

where, r_{ketone} is the measured reaction rate of the ketone or H_2 (mol $g^{-1}\ s^{-1}$), ρ_b is the packing density of the catalyst bed (g m^{-3}), R is the catalyst particle radius (in m; in this case we used R = 2.5 x 10^{-4} m), n the order of the reaction (we calculated the Mear's criterion assuming both first and second order reactions), k_c (m s^{-1}) the mass-transfer coefficient shown in eq. 2, D_{AB} the effective diffusivity of the ketone or H_2 in water (estimated using equation 3; Wilke and Chang 1955), Re the Reynolds number based on the particle size, Sc the Schmidt number ($\rho/[\mu D_{AB}]$), and C_{ketone} the bulk liquid phase concentration of the ketone or H_2 (mol m^{-3}).

$$k_c = 0.266\left(\frac{D_{AB}}{d_p}\right)\mathrm{Re}^{1.15}\ Sc^{1/3} \qquad (2)$$

$$D_{AB} = 1.17x^{-13}\left(\frac{\left(M_B\xi\right)^{1/2}T}{\mu_B V_A^{1/2}}\right) \qquad (3)$$

where μ_B is the viscosity of the solvent (centipoise or mPa*s), M_B is the molecular weight of the solvent, and ξ is the association factor of the solvent B (2.6 for water). The equation for k_c (eq. 2) was taken from Fogler, 1986 and is applicable for trickle beds with Re < 20 (Fogler, 1986; AICHE J. 1978, 24, 709). Our Reynolds number ranged from 0.02 to 0.2 using the Pd/C granules. The reaction rate for hydrogen was estimated based on the total moles of alcohols (isopropanol, 2-butanol, cyclopentanol) produced per mass of catalyst per time, assuming 1 mole of H_2 was consumed per mole of alcohol produced. The liquid phase concentration of H_2 was estimated using Henry's Law ($H = 4.48 \times 10^{-4}$ mol L^{-1} atm^{-1}) and assuming an ideal gas, where $H = 7.8 \times 10^{-4} * (-500*(1/T-1/298)$ mol/(L-atm) [Lide and Frederikse, 1995].

The Wiesz-Prater criterion (C_{WP}), eq. 4, was used to estimate the effect of internal mass transfer in the reactions with the catalysts (Fogler, 1986), where a $C_{WP} << 1$ indicates that internal (or intraparticle) mass transfer resistance can be ignored.

$$C_{WP} = \frac{-r_{ketone}\rho_p R^2}{D_{eff} C_{ketone,s}} \qquad (4)$$

R is the particle radius or path length for the ACM ($d_p = 0.50$ mm and $R=d_p/2$ for the granules; R = wall thickness/2 for ACM or 1.27×10^{-4} m), $-r\rho_p$ is the reaction rate per volume of catalyst, ρ_p is the measured catalyst packing density, and D_{eff} is the estimated effective diffusivity (~ 1.8-9 x 10^{-10} m^2 s^{-1}). The effective diffusivity, eq. 5, was estimated from the diffusion coefficient, the estimated particle porosity (ε = 0.2-0.5), and tortuosity factor (τ ~ 2-6 for activated carbon (Lua and Yang, 2009). We used a tortuosity factor, τ, of four and $\varepsilon = 0.5$ in our calculations for both Pd/C granules and Pd/ACM.

$$D_{eff} = \frac{D_{AB}\varepsilon_{particle}}{\tau_{particle}} \qquad (5)$$

S6.2 Activated Carbon Monolith

Our liquid superficial velocity varied from 1.64 to 13.3 x 10^{-5} m/s and the gas velocity was fixed at 3.3 x 10^{-3} m/s. Thus, the gas/liquid velocity ratio for our work ranged from 200 (lowest liquid velocity) to 12.5 (highest liquid velocity). This gas/liquid velocity ratio suggested our work was conducted in film or annular flow (Q_g/Q_l = 12.5 to 500), since Q_g/Q_l ratios of 0.2 to 2 are

reported to generate Taylor flow in monoliths (Mogalicherla et al., 2010; Kawakami et al., 1989; Bauer et al., 2005). There are three possible transport steps in a monolith reactor undergoing a gas-liquid-solid reaction with Taylor flow, 1) gas to solid (through a very thin film), gas to liquid (a liquid slug with circulating eddies), and from the liquid slug to the solid surface. Since our Q_g/Q_l ratio suggested we were in film flow, we assumed transport of H_2 was from the gas phase to the solid (through a thin film). Under these conditions the mass transfer coefficient was estimated using equation 5 and 6 (Han and Shikazono, 2009).

$$k_{GS} = \left(\frac{D_{AB}}{\delta_F} \right) \qquad (6)$$

$$\delta_F = 0.5 d_h \left(\frac{0.67 Ca_B^{\frac{2}{3}}}{1 + a1 + a2 - a3} \right) \qquad (7)$$

Where,

k_{GS} is the mass transfer coefficient; D_{AB} is the diffusivity of the ketone or H_2 in the liquid

δ_F is the film thickness; a1 = 3.13 x $Ca_B^{(2/3)}$; a2 = 0.504 x $Ca_B^{0.672}$ $Re^{0.589}$; a3 = 0.353 $We^{0.629}$

Ca_B is the capillary number for the bubbles, $(U_B\mu)/\sigma$; We is the Weber number, $d_H U^2 \rho/\sigma$; and Re < 2000; d_H = 0.3-1.3 mm; Ca_B = 0-0.38; U_B = bubble velocity (we assumed the gas velocity for the bubble velocity); d_H hydraulic diameter; ρ solvent density; σ surface tension of solvent

A summary of the key calculated data input for the Mears and Wiesz-Prater criterion are shown in Table S3.

S6.3 Literature Cited

Fogler, H.S., 1986. Elements of Chemical Reaction Engineering. Prentice-Hall, Englewood Cliffs, New Jersey.

Lide, D. R. and H. P. R. Frederikse, editors. CRC Handbook of Chemistry and Physics, 76th Edition. CRC Press, Inc., Boca Raton, FL, 1995.

Lua, A-C., Yang, T. Theoretical Analysis and Experimental Study on SO_2 Adsorption onto Pistachio-nut-shell Activated Carbon. 2009. AIChE Journal. 55, 2, 423.

Wilke, C.R., Chang, P. AIChE Journal.1955. 1, 264.

Bauer, T. et al., Trans IChemE, Part A, Chemical Engineering Research and Design, 2005, 83(A7): 811–819.

Kawakami, K.; Kawasaki, K.; Shiraishi, F.; Kusunoki, K. Performance of a honeycomb monolith bioreactor in a gas-liquid-solid three-phase system. Ind. Eng. Chem. Res., 1989. 28: 394–400.

Mogalicherla, A.K.; Kunzru, D. Effect of Gas and Liquid Superfical Velocities on the Performance of Monolithic Reactors. Ind. Eng. Chem. Res. 2010, 49, 1631–1641.

Haasea, S.; Yu., Murzin, D.Y.; Salmi, T. Review on hydrodynamics and mass transfer in minichannel wall reactors with gas–liquid Taylor flow. Chemical Engineering Research and Design. 113 (2016) 304–329.

Han, Y., Shikazono, N., Measurement of the liquid film thickness in micro tube slug flow. Int. J. Heat Fluid Flow. 2009. 30 (October (5)), 842–853.

Table S3: Estimated Mears criterion for Pd/C granules and Pd/ACM.

	Pd/C Granules					Pd/ACM						
Q_g/Q_l	LHSV (h^{-1})	kc, m/s CPON	Mears CPON	kc, m/s H_2	Mears H_2	LHSV (h^{-1})	δ m	kc, m/s CPON	Mears CPON	kc, m/s H_2	Mears H_2 n=2	Mears H_2 n=1
200	0.77	$1.2x10^{-3}$	$5.9x10^{-5}$	$3.7x10^{-3}$	$3.9x10^{-5}$	0.39	$1.9x10^{-7}$	$7.2x10^{-3}$	0.01	$3.7x10^{-3}$	0.07	0.04
100	1.54	$2.7x10^{-3}$	$4.8x10^{-5}$	$8.1x10^{-3}$	$11x10^{-5}$	0.78	"	$7.2x10^{-3}$	0.02	$3.7x10^{-3}$	0.14	0.07
66.7	-	-	-	-	-	1.2	"	$7.2x10^{-3}$	0.033	$3.6x10^{-3}$	0.196	0.1
50	3.1	$6x10^{-3}$	$4.6x10^{-5}$	$18x10^{-3}$	$8.8x10^{-5}$	-						
25	6.2	$13x10^{-3}$	$3.9x10^{-5}$	$40x10^{-3}$	$12x10^{-5}$	3.1	"	$7.1x10^{-3}$	0.058	$3.6x10^{-3}$	0.62	0.31
12.5	-	-	-	-	-	6.2	"	$6.9x10^{-3}$	0.14	$3.5x10^{-3}$	1.03	0.52

Q_g is gas flow rate; Q_l is liquid flowrate; CPON is cyclopentanone; LHSV = $(Q_l*\rho_B)/W_{cat}$; W_{cat} is amount of catalyst
$D_{AB(cyclopentanone)} = 1.36x10^{-9}$ m^2/s; $D_{AB\ (H2)} = 4.14x10^{-9}$ m^2/s
$D_{eff\ (cyclopentanone)} = 1.7x10^{-10}$ m^2/s; $D_{eff\ (H2)} = 5.2x10^{-10}$ m^2/s
Tortuosity Factor = 4; Internal Void Fraction = 0.5; n or reaction order = 2, except where noted
Bulk Liquid Phase Concentrations: $C_{CPON} = 0.096$ mol/L; $C_{H2} = 0.009$ mol/L
kc is the mass-transfer coefficient, m/s
δ is the film thickness, m
σ is surface tension and was assumed as 0.06 N/m (for water)
$\rho_B = 0.26$ g/ml, bulk density of Pd/C granules
$\rho_P = 0.28$ g/ml, packing density of Pd/ACM
$R = d_p/2$ for granules and Wall thickness/2 for ACM